## Morpho-structural criteria for the identification of spreading-induced deformation processes potentially comprising stratovolcano stability.
### --Manuscript Draft--

| Manuscript Number: | |
|---|---|
| Full Title: | Morpho-structural criteria for the identification of spreading-induced deformation processes potentially comprising stratovolcano stability. |
| Article Type: | Research Article |
| Corresponding Author: | M. Rincón<br>Universidad Rey Juan Carlos - Campus de Móstoles: Universidad Rey Juan Carlos<br>Móstoles, Madrid SPAIN |
| Corresponding Author Secondary Information: | |
| Order of Authors: | M. Rincón |
| | A. Márquez |
| | R. Herrera |
| | F. Martín-González |
| | I. López |
| | C. Crespo-Martín |
| Funding Information: | |
| Abstract: | The characterization of stratovolcanoes' surface deformation is essential for a better understanding of the processes that can compromise volcano structural stability and possible flank collapse. Morphological similarities produce by volcano deformation due to the presence of an hydrothermal core and by the intrusion of a viscous magma body, produce a pressing need for advancing in our understanding of recognition criteria of stratovolcanoes flank spreading. We provide analogue models and real volcanoes examples to characterize and recognize the surface deformation patterns produced by spreading due to the presence of an hydrothermal core. Our results show differences between spreading produced by the presence of an hydrothermal core and intrusion processes inside the volcano in: (1) a sharp transition between areas of subsidence and uplift is typical of intrusion-related deformation; (2) the development of faults with oblique strikes in the upper part occurs only at intrusion experiments; and (3) the development of flank bulging close to the cone base only occurs during asymmetric flank spreading. However, although laboratory results show different criteria representative of the spreading process, diagnostic ('forensic') application to real volcanoes is difficult, as in most cases some diagnostic structures cannot be preserved. The occurrence of "basal" bulging at an edifice arises as a potentially powerful diagnostic morphological feature for the identification of an asymmetric volcano flank spreading potentially compromising stratovolcanoes stability. Remote sensing techniques can allow the identification of such basal bulges, providing an easy tool for a more complete hazard assessment and refined monitoring strategy at potentially unstable volcanoes. |
| Suggested Reviewers: | Benjamin van Wyk de Vries<br>ben.vanwyk@uca.fr |
| | Benjamin van Wyk de Vries<br>ben.vanwyk@uca.fr |
| | Mark E Reid<br>mreid@usgs.gov |
| | Andrea Borgia<br>aborgia@lbl.gov |
| Author Comments: | |

1 **Morpho-structural criteria for the identification of spreading-induced deformation**

2 **processes potentially comprising stratovolcano stability.**

3

4 **M. Rincón[1], A. Márquez[1,2], R. Herrera[1], F. Martín-González[1], I. López[1], C. Crespo-Martín[1]**

5

6 *1 ESCET, Área de Geología, Tecvolrisk Research Group, Universidad Rey Juan Carlos,*

7 *Móstoles, Spain.*

8 *2 Departamento de Mineralogía y Petrología, Universidad Complutense, Madrid, Spain,*

10

11 Corresponding author: Marta Rincón Ramos (marta.rincon@urjc.es)

12

13

14

15

16

17

18

19

20

21

22    ABSTRACT

23    The characterization of stratovolcanoes' surface deformation is essential for a better understanding of the

24    processes that can compromise volcano structural stability and possible flank collapse. Morphological

25    similarities produce by volcano deformation due to the presence of an hydrothermal core and by the

26    intrusion of a viscous magma body, produce a pressing need for advancing in our understanding of

27    recognition criteria of stratovolcanoes flank spreading. We provide analogue models and real volcanoes

28    examples to characterize and recognize the surface deformation patterns produced by spreading due to the

29    presence of an hydrothermal core. Our results show differences between spreading produced by the

30    presence of an hydrothermal core and intrusion processes inside the volcano in: (1) a sharp transition

31    between areas of subsidence and uplift is typical of intrusion-related deformation; (2) the development of

32    faults with oblique strikes in the upper part occurs only at intrusion experiments; and (3) the development

33    of flank bulging close to the cone base only occurs during asymmetric flank spreading. However, although

34    laboratory results show different criteria representative of the spreading process, diagnostic ('forensic')

35    application to real volcanoes is difficult, as in most cases some diagnostic structures cannot be preserved.

36    The occurrence of "basal" bulging at an edifice arises as a potentially powerful diagnostic morphological

37    feature for the identification of an asymmetric volcano flank spreading potentially compromising

38    stratovolcanoes stability. Remote sensing techniques can allow the identification of such basal bulges,

39    providing an easy tool for a more complete hazard assessment and refined monitoring strategy at potentially

40    unstable volcanoes.

41

42

43

44

45

46

47

48

INTRODUCTION

50     Catastrophic flank collapse can occur in any volcano type, independent of its composition, shape, size, or

51     geodynamic context (McGuire 1996; Acocella 2005; Carrasco-Nuñez et al. 2011). Interest has been given

52     to the instability and catastrophic flank collapse of stratovolcanoes, especially since Mt. St. Helens'

53     eruption in 1980 (e.g., Voight et al. 1983; Siebert 1992; Carrasco-Nuñez et al. 2011). Flank collapse at

54     stratovolcanoes must be considered a strongly hazardous process, both due to its ability to potentially

55     impact large areas (including those affected by secondary hazards, as tsunamis) and to its high temporal

56     frequency, having caused about 20,000 fatalities in historical times (Siebert et al. 1987). Since 1500 AD,

57     25 flank collapses involving a volume of material greater than 0.1 $km^3$ have been recorded in

58     stratovolcanoes (Carrasco Nuñez et al. 2011): a frequency of 4-5 times per century.

59     From those 25 large historic volcanoes' catastrophic flank collapses, 16 were associated with a coetaneous

60     magmatic activity (64%), whereas 4 of them were related to phreatic explosions, and in 5 cases no explosive

61     component was identified (Carrasco-Núñez et al. 2011). The close connection between magma intrusion

62     and catastrophic lateral collapse in volcanic edifices is confirmed in the geological record by numerous

63     examples where volcanic debris avalanche deposits contain juvenile magmatic clasts or directly overlie

64     nearly simultaneous explosive deposits (Belousov et al. 2007). However, even though most of the identified

65     volcanic flank collapses, including the historical cases, were induced by a magmatic intrusion (e.g., St.

66     Helens at 1980; Voight et al. 1983), the geological record also shows numerous examples of the occurrence

67     of volcanic debris-avalanche deposits with no magmatic component or eruptive deposit associated (e.g.,

68     the historic cases of Mombacho (Nicaragua) at AD 1540 or Unzen (Japan) at AD 1792; van Wyk de Vries

69     and Francis 1997; Siebert et al. 1987). The prime factors for stratovolcano instability in these cases of no-

70     magmatic collapses have been frequently related to other internal geological processes, such as: 1) the

71     action of faults underlying the volcanic edifice (e.g., Lagmay et al. 2000); 2) the asymmetric volcano

72     spreading over a weak basal layer (Borgia et al. 1992; Borgia and van Wyk de Vries 2003) or 3) the

73     development of a core of hydrothermally altered rocks inside the volcano (van Wyk de Vries et al. 2000).

74     Hydrothermal rock alteration probably plays a key role as a priming mechanism for stratovolcano instability

75     and lateral catastrophic collapses, as evidenced by: 1) the presence of hydrothermally altered material in

76     several volcanic debris avalanche deposits (e.g., Pevear 1982; Voight et al. 2002; Salaün et al. 2011), and

77     2) the association of hydrothermal explosions with several historical examples of catastrophic flank

78  collapse (Reid et al. 2001). For example, at the Bandai volcano (Japan) in AD 1888, successive phreatic

79  eruptions (up to 20 times a minute) occurred until the final one triggered the catastrophic collapse of the

80  volcano's northern flank (Sekiya and Kikuchi, 1980). The significant number of stratovolcanoes worldwide

81  showing surface evidence of a hydrothermal system inside (hot water and/or gases emissions,

82  hydrothermally altered zones) underlies the relevance of these processes in analysing potential collapse-

83  related hazards.

84  The role of hydrothermal alteration for making unstable a volcanic edifice is manifold. First, alteration of

85  the volcanic rocks can reduce the porosity and permeability of the rocks (Berger and Henley 2011; Horwell

86  et al. 2013) promoting the development of high pore fluid pressures within the volcanic edifice, which can

87  favour fracturing and therefore a loss of strength (Lopez and Williams 1993; Day 1996; Reid 2004; Heap

88  et al. 2021). Furthermore, hydrothermally altered rocks become mechanically weaker than fresh rocks due

89  to the development of secondary minerals (mainly clay minerals), which have low strengths and reduce

90  cohesion and friction values of the rock mass (Darmawan et al. 2020). In addition, altered rocks show a

91  tendency to deform mainly by ductile mechanisms, so the development of such a weak and ductile core of

92  hydrothermally altered rocks can promote the gradual spreading of the edifice (van Wyk de Vries et al.

93  2000; Cecchi et al. 2004). This ductile deformation can show very low-rates, challenging its detection by

94  geodetic monitoring techniques (InSar or GPS).

95  The understanding in stratovolcanoes subjected to hydrothermal activity of the factors that promote their

96  catastrophic flank collapse, as well as the identification of diagnostic deformation features, can save lives

97  and property. Some insights into the volcano instability process due to the development of a weak

98  hydrothermal core have been obtained from field observations (Rosas Carbajal et al. 2016), remote sensing

99  (Michon and Saint- Ange, 2008), rock mechanics (Zimbelman et al. 2003) and numerical modelling

100 (Kelfoun et al. 2021), but key contributions for the identification and understanding of this process have

101 come from analogue modelling (Cecchi et al. 2004; van Wyk de Vries et al. 2000; Andrade and van Wyk

102 de Vries 2010; Rincón et al. 2015; Rincón et al. 2018).

103 In this way, analogue modelling has shown that the development of a concave-convex shaped flank at

104 stratovolcanoes can be considered as one of the most characteristic diagnostic features of the occurrence of

105 a gradual asymmetric gravitational deformation of weak-cored edifices. For this reason, at several

106 volcanoes has been proposed as evidence of the flank spreading of the edifice (e.g., Semeru volcano,

4

107   Indonesia; Solikhin et al. 2012). However, analogue modelling, as well as observations of some historical

108   episodes (e.g., Bezymianny, Kamchatka, at 1959 or St. Helens, USA, in 1980), have shown that a

109   cryptodome intrusion can also produce the volcano flank bulging developing a concave-convex profile

110   (Donnadieu et al. 2003, Cecchi et al. 2004). Those deformation features, which can be potentially quite

111   similar to those proposed as diagnostic of an active flank spreading, can be preserved for some time in the

112   volcano surface (e.g., van Wyk de Vries et al. 2018); i.e., an old intrusion can potentially have shaped the

113   volcano a long time ago in a way that strongly resembles the morphology of an edifice suffering an active

114   flank spreading (Donnadieu et al. 2003).

115   For this reason, in order to improve our ability to identify if the deformation mechanism responsible for

116   flank bulging of a stratovolcano flank is an active slow spreading (i.e., undetected for monitoring systems)

117   or the past deformation due to an old intrusion, we propose that a set of diagnostic criteria is needed based

118   on the morphology and the deformation structures observable on the volcano surface. To constrain those

119   morphological diagnostic criteria, we have performed an experimental study using systematically

120   comparable analogue models of volcano deformation due to a weak core and a viscous magma intrusion.

121

122   3. EXPERIMENTAL METHODOLOGY

123   *3.1.* Experimental setup

124   We have made two different types of volcano deformation models: 1) Type S which recreates volcano

125   spreading process due to the existence of a hydrothermal weak core; and 2) Type I which recreates a

126   cryptodome (i.e., viscous magma) intrusion. A mixture of fine-grained sand (80%) and plaster (20%) has

127   been used to simulate the fresh rock of the volcanic edifice at both types of models. This granular material

128   is commonly used to modeling crustal volcanic rock and visualize brittle faulting (e.g., Merle and Borgia

129   1996; Delcamp et al. 2008; Rincón et al. 2015; Rincon et al. 2018).  In both setups, the cones have been

130   constructed on a rigid base above a one-centimetre-thick layer of the same material as the cone, in order to

131   avoid the process of friction between the sand cone and the rigid surface (figure 1). In the first setup (type

132   S) the core formed by hydrothermally altered rock has been simulated with silicone FB GUM, following

133   the methodology of Cecchi et al. (2004). The second type of model (type I) reproduces magmatic intrusion

134   processes using syrup injected from the base of stratovolcanoes with the same methodology as Rincón et

135    al., 2018 (figure 1). We use a Microsoft® Kinect v2 sensor in all the experiments for monitoring the surface

136    deformation (Rincón et al. 2018, 2022) (figure 1).

137    In type S experiments, due to the diversity of possible shape, size, and locations of the hydrothermal cores

138    inside stratovolcanoes, we design of experiments set to systematically recreate spreading caused by the

139    presence of a hydrothermal core with different characteristics. We consider three different variables for the

140    weak core; (1) core shape: cube, prism and cone; (2) core size: large (10%) and small (5%); and (3) core

141    position: base - centre, medium - centre and base - side (Figure 2). The combination of these three variables

142    results in 17 possible different experimental settings that reproduce the different possible occurrences of a

143    weak core inside a volcano (Figure 2). In order to validate the reproducibility of these S experiments, the

144    experiment S6 has been repeated 9 times; the variability observed in the morphology and faults due to the

145    cone deformation is minimal and the main diagnostic features appear at all the test (Online Resource 1).

146    On the other hand, we have realized a set of 6 experiments of type I. The only variable in these experiments

147    was the distance between the intrusion tube and the central axis of the cone: we show here experiments

148    with distances less than 0.5 cm and distances between 1.5-3 cm. The results from the I-experiments

149    performed are alike to those obtained by Rincón et al. (2018).

150

151    *3.2.* Scaling and materials

152    In order to compare surface changes and faults patterns in the analogue models with field data in the natural

153    systems, scaling of the experiments needs to be geometrically, dynamically, and kinetically defined

154    (Hubbert 1937). For the scaling in this work, the method and the range of the parameters are the same used

155    by Rincón et al. (2018). The length scale $[L]^*$ is $10^{-4}$ (so 10 m in real volcanoes is 1 mm in the model). The

156    cone height (hM) is 11 cm, modelling an 1100 m edifice (hN). The cohesion of the model material (σM)

157    has been estimated by shear-ring test in HelTec Lab of GFZ Potsdam (Samaniego et al. 2015), obtaining

158    values of 50-100 Pa, which simulates a fresh rock mass with a cohesion (σN) of $9 \cdot 10^5$ - $2 \cdot 10^6$ Pa ($\approx 1 - 2$

159    MPa) (Seisdedos et al. 2012).

160    To simulate the hydrothermally altered volcanic core we employ the Rhodorsil GUM FB® silicone because

161    of the tendency of the hydrothermally altered rocks to deform mainly by creep (van Wyk de Vries et al.

162    2000; Cecchi et al. 2004). The viscosity of Rhodorsil FB® silicone is $1 \cdot 10^4$ Pa·s (Calvin et al. 2013)

163    whereas the viscosity of a real hydrothermal core has been estimated around $1 \cdot 10^{18}$ Pa·s (van Wyk de Vries

6

164 and Matela 1998). In this way, one minute of a type S experiment corresponds to around 10,0000 years at

165 nature. In our type-I experiments we used Lylle's Golden Syrup to simulate the intrusion of magmas with

166 viscosities around $1·10^9$ Pa·s, like those proposed for the cryptodome of Mt. St. Helens in 1980 (Pinkerton

167 and Stevenson 1992). Therefore, and according to the defined scaling (Table 1), our model flows ($Q_M$) of

168 ~2 cm$^3$/s are properly modelling natural flows ($Q_N$) of ~30 m$^3$/s, similar also to that of the Mt. St Helens

169 cryptodome intrusion at 1980 (Moore and Albee 1981).

170 *3.3.* Data analysis

171 Experiments are monitored using the RGB and distance images obtained by the sensor Kinect v2 of

172 Microsoft® (Rincón et al. 2020). We used the RGB images to map the deformation structures (faults). With

173 the distance images we can quantify the topographic changes of simulated stratovolcanoes throughout the

174 several temporal stages of the process. Spatial resolution are 1920 x 1080 pixels for RGB images and 512

175 x 420 pixels for the distance images. Since we record data from a height of 75 cm, the pixel sizes are 0.6

176 mm and 1.6 mm respectively. Temporal resolution is 1 image per second recorded every 10 minutes during

177 type S experiments and 1 image per second until the syrup reached the surface at type I experiments.

178 To obtain quantitative values of the surface deformation (i.e. subsidence and/or bulge) of the cone during

179 the experiments, we calculate the difference between the values of the different acquired distance images

180 and that of the starting time of the experiment (t0). For type S experiments we analyse the images of the

181 minutes 1 (t1), 2 (t2) y 3 (t3), which correspond approximately to 10000, 20000, and 30000 years in nature,

182 according to scaling. The selected times for type I are 5 (t5), 10 (t10), and 20 (t20) minutes in the

183 experiment, representing 6, 12, 19, and 25 days in nature approximately.

184

185 4. RESULTS FROM ANALOGUE MODELS

186 4.1. Deformation by spreading due to a hydrothermal weak core (S-type models).

187 Most of the S-type models show a visible deformation at the cone surfaces, both as topographic

188 displacements and faulting (Figure 3). The greater and closer to the surface is the weak core simulating the

189 hydrothermally altered rocks body, the larger and more intense is the surface deformation (Figure 3).

190 Surface morphology changes detected are mainly characterized by the subsidence of the summit area (up

191 to 15 mm), developing a characteristic summit flat (i.e., low-slope) area at the edifice (Figures 3 and 4). In

192 several experiments, this subsidence is accompanied by a partially surrounding zone of small positive

193 displacements which, even in those cases where the weak core is located centred in the cone, can show a

194 small asymmetry with larger developments in different flanks (see experiments S1, S2, S10, S11, S14 and

195 S17 at figure 3). Faulting pattern at most of those centred cases is symmetrical, with the development of

196 two main curved normal faults, bounding the subsidence zone, dipping to the centre of the cone forming a

197 summit graben structure (see experiments S1, S2, S10, S11, S14 and S17 at figure 3).

198 In most of the models where the weak core is located off-centre in the edifice, faulting pattern changes: an

199 early master curved normal fault, located at the flank opposite to the weak core, develops dipping inward

200 the edifice (Figure 3: all the off-centre experiments except S3). In the hanging wall of this master fault, one

201 or several minor antithetic normal faults develop generating a half-graben structure in a highly deformed

202 flank. In addition, a prominent (up to 25 mm of positive displacement) topographic bulge growth close to

203 the cone base downslope of the fault system, presumably related to the development of a blind gently

204 dipping inverse fault at its base. This bulged area extends for around 1/4 of the edifice diameter, as a

205 minimum, even for narrow weak-cores (e.g., experiment S12 at figure 3). Remarkably, the maximum

206 subsidence is again located at the cone summit area, although extending into the deformed flank. The

207 deformed flank develops a topographic profile with a characteristic concave-convex shape (see experiments

208 S3, S6, S9, S12, S15 and S18 at figure 4), which has been already suggested as indicative of volcano flank

209 spreading (van Wyk de Vries and Francis 1997; van Wyk de Vries and Matela 1998)

210 In summary, surface deformation in off-centre S-models shows a quite distinctive asymmetrical pattern:

211 intense faulting forming an asymmetrical half-graben affecting the upper-half part of the flank, which

212 downslope shows a prominent bulge near the cone base, resulting in a concave-convex shape of the cone

213 flank (see experiments S3, S6, S9, S12, S15 and S18 at figures 3 and 4). We suggest that the deduced

214 geometry of those faults inside the edifice results in a strong potential instability of that deformed flank,

215 which therefore becomes prone for its catastrophic lateral collapse.

216

217 4.2. Comparison with deformation due to the intrusion of a viscous magma body (I-type models).

218 Surface deformation patterns detected at cones affected by the intrusion of a simulated viscous magma body

219 shows several features apparently similar to those at S-models. In our I-type models deformation is also

220  different between cases where the tube intrusion is centred or off-centred respect to the cone summit, in

221  agreement with previous results from Rincon et al. (2018). When intrusion occurred right beneath the cone

222  summit, edifice faulting is mainly symmetrical with two main inward-dipping normal faults forming a

223  summit graben, characterized by subsidence surface displacements. In some cases, the footwall zone of one

224  of the faults delimiting the graben also shows a small positive displacement (i.e., bulging. See experiment

225  I33, I35 e I44 at figure 5). That deformation pattern is quite similar to that from the S-models with the weak

226  core centred inside the cone (see experiments S1, S2 at figure 3)

227  However, in the cases when the intrusion occurs below one flank (i.e., off-centre), cone deformation shows

228  a completely different pattern, with the early development of a curved normal fault perpendicular to the

229  intruded flank dipping inward the volcano, producing a summit asymmetric half-graben with large and

230  strong (up to 25 mm) subsidence at the master fault hanging wall. The maximum subsidence zone can

231  therefore occur not at the cone summit zone, but slightly displaced (i.e., above of the intrusion point) (see

232  experiments I4, I18 and I40 at figure 5). Remarkably, a topographic bulge appears at the intruded flank, in

233  sharp transition with the subsidence zone (in some cases clearly bounded by one the graben faults), and

234  therefore always at the upper-middle zone of the flank, but not at the cone base (see topographic profile of

235  experiment I4 at figure 6). This deformation pattern can be therefore very similar to that from some of the

236  off-centre S-models, except in the location of the bulge (upper-middle flank vs. cone base) (e.g., experiment

237  S12 at figure 4 vs experiment I4 at figure 6).

238  Another remarkable deformation characteristic observed in these off-centred I-models is the development

239  at the hanging-wall block of normal faults trending ≈ 30˚ respect to the first master fault (see experiments

240  I4 and I18 at Figure 5). This faulting pattern appears at advanced times of the experiment. Occasionally,

241  also a late "slump-like" structure develops, defined by a U-shaped normal fault and a prominent bulge,

242  trending highly oblique to the first larger master fault (see experiments I4 and I40 at Figure 5).

243  5. DISCUSSION

244  5.1. Morpho-structural features indicative of potential volcano instability due to flank spreading.

245  Our S-type experiments, simulating the gravitational deformation of a stratovolcano with a weak core of

246  hydrothermally altered rocks, show how a volcanic edifice can spread developing faulting patterns which

247  potentially can compromise its stability: a normal master fault involving a large portion of the edifice,

248  including a strongly deformed flank. This asymmetrical unstable deformation of the volcano by preferential

249    flank spreading is only observed in some of the models where the weak core is located off-centred, in

250    agreement with results from previous models of Cecchi et al. (2004). Additionally, our models show that

251    this volcano deformation can occur even when the weak hydrothermally-altered core is only 5% in volume

252    in the edifice (10% for Cecchi et al. 2004), showing that even quite small hydrothermal systems can

253    potentially generate instability in stratovolcanoes.

254    One of the most characteristic topographic features observed in our models due to the cone spreading over

255    its weak core is the development of a flat (low-slope) summit area due to edifice subsidence. That flat

256    summit area could therefore potentially become a good evidence for identifying the spreading of a

257    stratovolcano. However, that graben-like flat area can be difficult to identify since lava flows from central

258    vent can infill it and even cover and mask the topographic scarps produced by faulting. In any case, since

259    both the symmetrical and asymmetrical (i.e., restricted to a flank) spreading of the edifice produce

260    subsidence at the summit area, this criterion is not useful for the identification of a potential instability of a

261    stratovolcano. Similarly, if the deformation of the volcano was due to an old intrusion of a viscous magma

262    body, our I-models show that a graben-like flat area due to topographic subsidence develops also at the

263    cone summit zone.The occurrence of a flat summit area in a stratovolcano is therefore a useless criterion

264    for characterizing volcano deformation process.

265    Otherwise, other topographic characteristic diagnostic of volcano deformation detected in our experiments,

266    the flank bulging signature, can be detected even if later lava flows cover the area, due both to the change

267    in slope and also by the potential change in morphology of the later flows reaching the slope-change area.

268    Both flank spreading and intrusion processes can produce a bulge at the edifice (see Figures 3, 4, 5 and 6).

269    Our results show that a fault-related sharp transition between subsidence and uplift at deformed volcano

270    flanks is typical of intrusion-related deformation. This distinctive feature occurs in all our experiments,

271    strengthening the proposal made by Donnadieu et al (2003) using only one experiment as well as previous

272    field observations (e.g., van Wyk de Vries et al. 2014).

273    In addition, our I-type experiments show that the deformation due to a viscous magma intrusion high in the

274    edifice can derive in a characteristic and diagnostic faulting pattern, with the development of faults with

275    different strikes crosscutting in the upper part of the deformed flank (Figure 5). This faulting pattern appears

276    therefore as a potentially very powerful criterion for the recognition of past edifice deformation by an old

277    intrusion, and therefore for discarding an active volcano flank spreading in an edifice which shows

278     morphological features such as a flat summit area and a concave-convex flank. However, we have no found

279     evidence of that faulting pattern at any volcano worldwide, neither at our analysis of satellite images (see

280     Section 5.2.) nor at the scientific literature. This faulting pattern occurs in our experiments at a late stage,

281     when the intrusion is probably located high in the edifice above the main fault plane, and therefore the

282     volcano is in a highly unstable stage (Rincón et al., 2018). Therefore, we propose that this faulting pattern

283     is highly improbable to be preserved at stratovolcanoes at nature due to the probable catastrophic lateral

284     collapse of the edifices at those situations.

285     Finally, the comparative analysis of our S- and I-type models shows that the volcano flank bulging close to

286     the cone base only occurs in those cases where the edifice is suffering an asymmetric spreading (see

287     experiments S6, S9, S12, S15 and S18 at Figures 3 and 4). The development of "basal" bulging of the

288     edifice arises therefore as a diagnostic morphological feature for the identification of an asymmetric

289     volcano flank spreading which potentially can be compromising the edifice stability in that sector

290

291     5.2. Application to natural cases

292     Volcano flank bulging, with the development of a characteristic concave-convex-concave profile at the

293     edifice deformed flank, has been previously proposed as a morphological criteria for identifying the

294     development of flank spreading at several volcanoes; e.g.: Casita (van Wyk de Vries et al., 2000),

295     Mombacho (Cecchi et al., 2004), Piton de la Fournaise (Carter et al., 2007), Teide (Márquez et al., 2008),

296     Semeru (Solikhin et al., 2012) or Damavand (Eskandari et al., 2015). The surface occurrence of

297     hydrothermally altered rocks at several of those volcanoes (Casita, Teide, Damavand) strongly supports

298     that the volcano flank spreading can be produced by the existence of a core of weak rocks in the edifice.

299     Applying our described morphological criteria to proposed examples of volcano flank spreading some

300     noticeable features appear, in some cases providing new arguments for the existing controversies about the

301     role of flank spreading.

302     At Casita volcano (Nicaragua) the topographic profile across the proposed deformed east flank (van Wyk

303     de Vries et al., 2000) shows strong similarities to some of our cases of spreading due to a weak core located

304     centred in the cone, with a convex part located at the middle flank (Figure 8). That structural setting is not

305     potentially such unstable as the case where the weak core is located off-centre in the volcano. Even through,

306     the induced flank steeping and head scar faulting can produce small landslides which can transform into

11

307  small debris avalanches or lahars, as occurred at the edifice SE flank at 1998 (Kerle & van Wyk de Vries,

308  2001). That landslide left a small horse-shoe scarp in the volcano flank (Figure 8

309

310  Damavand volcano (Iran) shows some similar features, with a a characteristic concave-convex-concave

311  shaped SE flank (Figure 8) bounded at the north by a shallow horse-shoe scarp. That E-SE flank of the

312  edifice is actively deforming several millimetres per year to the west-down at the upper concave flank

313  sector, and west-down at the convex zone, according to InSAR data (Shirzaei et al., 2011; see their Figure

314  3). That deformation pattern is similar to that occurring in our models with a small off-centred weak core

315  (see e.g., S6 or 18 at Figure 3). These observations suggest that Damavand south-eastern flank can be

316  potentially unstable due to an asymmetric flank spreading process, constituting a threat of possible collapse

317  for the village of Ask and other localities at the Haraz River valley at the south-east foot of the volcano.

318  The morphology of the edifice flank also supports the proposal of Cecchi et al. (2004) that some of the

319  shallow horse-shoe structures occurring at volcano flanks can have been induced by flank spreading and

320  thus become a diagnostic feature of edifice deformation and instability.

321  According to our models, Semeru volcano (Indonesia) stability can be compromised due to south-directed

322  flank spreading, since the alleged bulge is located close to the base of the edifice flank (figure 8; see also

323  Figure 9 of Solikhin et al., 2012). However, after our inspection of volcano slope map, we have further

324  doubts about the existence of a deformation-related bulge at the edifice base, since the change-in-slope

325  defining the alleged southern bulge is quite small, discontinuous and lobate; i.e., it is not extended across a

326  significant part of the edifice base.

327  Additionally, we have made a preliminary survey using bibliography and the worldwide available SRTM

328  and Aster-DEM digital elevation models, looking for other possible examples of stratovolcanoes showing

329  morphological features potentially indicative of flank spreading (i.e., concave-convex-concave flanks,

330  possibly related to shallow horse-shoe structures). The most notable example found is Ubinas volcano

331  (Ecuador), where also a concave-convex-concave shaped flank (with an area ~2 x 1 km) bounded by a

332  horse-shoe scarp occur at volcano southeast side (Figure 8). The horse-shoe scarp is attributed to the

333  occurrence of a large sector collapse occurred at the volcano around 3,670 yr. B.P. involving

334  hydrothermally altered blocks (Thouret et al., 2005). Ubinas edifice has a well-developed hydrothermal

335  system with a south-eastern trend asymmetric distribution (Gonzales et al., 2014). In fact, Ubinas is

336 considered a highly unstable volcano at its south flank, and the possibility of a flank failure of that

337 hydrothermally-altered zone affecting the area of the previous collapse is yet considered in the possible

338 eruptive scenarios in the hazards assessment (Thouret et al. 2005). However, it must be noted that the

339 morphology and structure of the flank adjacent at the NE to the horse-shoe scarp fit with our models where

340 a large off-centre weak-core is located inside the cone (see e.g. models S9 or S15 at Figure 3, compared to

341 profile at Figure 8). This suggests that the area where volcano stability can be compromised is larger than

342 the considered at the current volcano hazards map (Thouret et al. 2005, Rivera et al. 2010), and that a flank

343 collapse of a larger sector of the SE flank, including the area upslope of the Ubinas town, constitutes a

344 hazard that must be considered. Therefore, even although the previous monitoring of possible volcano flank

345 deformation at Ubinas using InSar techniques have not shown any signal (e.g., Rivera et al., 2010) we

346 suggest that the detailed monitoring of a potential slow long-term gravitational deformation at this SE

347 volcano flank is required due to the high potential hazard of a large catastrophic lateral collapse suggested

348 by the volcano morpho-structural criteria.

349

350 6. CONCLUSIONS

351 - Our experiments show that both the existence of a hydrothermal altered weak core or the intrusion

352 of a viscous magma body can produce two different deformation patterns at stratovolcanoes,

353 symmetric and asymmetric. Asymmetric deformation patterns can induce the instability of the

354 deformed volcano flank volcano producing structures that potentially can trigger its catastrophic

355 collapse.

356

357 - We identify three morpho-structural criteria which can potentially discriminate between

358 asymmetric volcano deformation due to spreading by a weak hydrothermal core or by intrusion of

359 a viscous magma body: (1) a sharp transition between areas of subsidence and uplift is typical of

360 intrusion-related deformation; (2) the development of faults with oblique strikes crosscutting in

361 the upper part of the deformed flank occurs only at intrusion experiments; and (3) the development

362 of flank bulging close to the cone base only occurs during asymmetric flank spreading.

363

364 - Diagnostic application of these criteria to natural cases seems to be hampered due to the usual

365 catastrophic lateral collapse of the stratovolcanoes deformed by off-centred viscous intrusions,

366 which erased the late-stage characteristic faulting patterns observed in our experiments.

13

367
368　　-　The development of "basal" bulging of the edifice arises therefore as the main diagnostic

369　　　　morphological feature for the identification of an asymmetric volcano flank spreading potentially

370　　　　compromising stratovolcanoes stability.

371
372　　-　The search and characterization of such basal bulges at stratovolcano flanks by remote sensing

373　　　　techniques can provide an easy tool for a more complete hazard assessment and refined monitoring

374　　　　strategy at potentially unstable volcanoes.

375

379

380　**REFERENCES**

381　Acocella, V. (2005). Modes of sector collapse of volcanic cones: Insights from analogue
382　experiments. Journal of Geophysical Research: Solid Earth, 110(B2).

383

384　Andrade, S. D., & van Wyk de Vries, B. (2010). Structural analysis of the early stages of catastrophic
385　stratovolcano flank-collapse using analogue models. Bulletin of Volcanology, 72(7), 771-789.

386

387　Belousov, A., Voight, B., & Belousova, M. (2007). Directed blasts and blast-generated pyroclastic density
388　currents: a comparison of the Bezymianny 1956, Mount St Helens 1980, and Soufrière Hills, Montserrat
389　1997 eruptions and deposits. Bulletin of Volcanology, 69(7), 701-740.

390

391　Berger, B. R., & Henley, R. W. (2011). Magmatic-vapor expansion and the formation of high-sulfidation
392　gold deposits: Structural controls on hydrothermal alteration and ore mineralization. Ore Geology
393　Reviews, 39(1-2), 75-90.

394　Borgia, A., Ferrari, L., & Pasquarè, G. (1992). Importance of gravitational spreading in the tectonic and
395　volcanic evolution of Mount Etna. Nature, 357(6375), 231-235.

396　Borgia, A., & van Wyk de Vries, B. (2003). The volcano-tectonic evolution of Concepción,
397　Nicaragua. Bulletin of Volcanology, 65(4), 248-266.

398

399　Calvín, P., Santolaria, P., Román Berdiel, T., & Tierz, P. (2013). Aportaciones de la modelización analógica
400　al estudio de la deformación intraplaca (No. ART-2013-79626).

401

402 Carrasco-Núñez, G., Siebert, L. & Capra, L. Hazards from volcanic avalanches. In Horizons in Earth

403 Science Research (eds Veress, B. & Szigethy, J.) 3, 199–227 (Nova Science Publishers, 2011).

404

405 Carter, A., van Wyk de Vries, B., Kelfoun, K., Bachèlery, P., & Briole, P. (2007). Pits, rifts and slumps:

406 the summit structure of Piton de la Fournaise. Bulletin of Volcanology, 69(7), 741-756.

407 Cecchi, E., van Wyk de Vries, B., & Lavest, J. M. (2004). Flank spreading and collapse of weak-cored

408 volcanoes. Bulletin of Volcanology, 67(1), 72-91.

409 Day, S. J. (1996). Hydrothermal pore fluid pressure and the stability of porous, permeable

410 volcanoes. Geological Society, London, Special Publications, 110(1), 77-93.

411 Darmawan, H., Yuliantoro, P., Rakhman, A., Santoso, A. B., Humaida, H., & Suryanto, W. (2020).

412 Dynamic velocity and seismic characteristics of gravitational rockfalls at the Merapi lava dome. Journal of

413 Volcanology and Geothermal Research, 404, 107010.

414 Delcamp, A., de Vries, B. V. W., & James, M. R. (2008). The influence of edifice slope and substrata on

415 volcano spreading. Journal of Volcanology and Geothermal Research, 177(4), 925-943.

416 Donnadieu, F., Kelfoun, K., de Vries, B. V. W., Cecchi, E., & Merle, O. (2003). Digital photogrammetry

417 as a tool in analogue modelling: applications to volcano instability. Journal of Volcanology and Geothermal

418 Research, 123(1-2), 161-180.

419

420 Eskandari, A., De Rosa, R., & Amini, S. (2015). Remote sensing of Damavand volcano (Iran) using Landsat

421 imagery: Implications for the volcano dynamics. Journal of Volcanology and Geothermal Research, 306,

422 41-57.

423

424 Gonzales, K., Finizola, A., Lénat, J. F., Macedo, O., Ramos, D., Thouret, J. C., ... & Pistre, K. (2014).

425 Asymmetrical structure, hydrothermal system and edifice stability: The case of Ubinas volcano, Peru,

426 revealed by geophysical surveys. Journal of Volcanology and Geothermal Research, 276, 132-144.

427

428 Heap, M. J., Baumann, T., Gilg, H. A., Kolzenburg, S., Ryan, A. G., Villeneuve, M., ... & Clynne, M. A.

429 (2021). Hydrothermal alteration can result in pore pressurization and volcano instability. Geology, 49(11),

430 1348-1352.

431

432 Horwell, C. J., Williamson, B. J., Llewellin, E. W., Damby, D. E., & Le Blond, J. S. (2013). The nature and

433 formation of cristobalite at the Soufrière Hills volcano, Montserrat: implications for the petrology and

434 stability of silicic lava domes. Bulletin of Volcanology, 75(3), 1-19.

435 Hubbert, M. K. (1937). Theory of scale models as applied to the study of geologic structures. Bulletin of

436 the Geological Society of America, 48(10), 1459-1520.

437 Kelfoun, K., Santoso, A. B., Latchimy, T., Bontemps, M., Nurdien, I., Beauducel, F., ... & Gueugneau, V.
438 (2021). Growth and collapse of the 2018–2019 lava dome of Merapi volcano. Bulletin of
439 Volcanology, 83(2), 1-13.

441 Kerle, N., & De Vries, B. V. W. (2001). The 1998 debris avalanche at Casita volcano, Nicaragua—
442 investigation of structural deformation as the cause of slope instability using remote sensing. Journal of
443 Volcanology and Geothermal Research, 105(1-2), 49-63.

445 Lagmay, A. M. F., Van Wyk de Vries, B., Kerle, N., & Pyle, D. M. (2000). Volcano instability induced by
446 strike-slip faulting. Bulletin of Volcanology, 62(4), 331-346.

448 López, D. L., & Williams, S. N. (1993). Catastrophic volcanic collapse: relation to hydrothermal
449 processes. Science, 260(5115), 1794-1796.

451 Márquez, A., López, I., Herrera, R., Martín- González, F., Izquierdo, T., & Carreno, F. (2008). Spreading
452 and potential instability of Teide volcano, Tenerife, Canary Islands. Geophysical Research Letters, 35(5).

454 McGuire, W. J. (1996). Volcano instability: a review of contemporary themes. Geological Society, London,
455 Special Publications, 110(1), 1-23.

457 Merle, O., & Borgia, A. (1996). Scaled experiments of volcanic spreading. Journal of Geophysical
458 Research: Solid Earth, 101(B6), 13805-13817.

460 Michon, L., & Saint- Ange, F. (2008). Morphology of Piton de la Fournaise basaltic shield volcano (La
461 Réunion Island): Characterization and implication in the volcano evolution. Journal of Geophysical
462 Research: Solid Earth, 113(B3).

463 Moore, J. G., & Rice, C. J. (1984). Chronology and character of the May 18, 1980, explosive eruptions of
464 Mount St. Helens. Explosive volcanism: inception, evolution, and hazards, 10, 133-157.

466 Pevear, D. R., Dethier, D. P., & Frank, D. (1982). Clay minerals in the 1980 deposits from Mount St.
467 Helens. Clays and Clay Minerals, 30(4), 241-252.

469 Pinkerton, H., & Stevenson, R. J. (1992). Methods of determining the rheological properties of magmas at
470 sub-liquidus temperatures. Journal of Volcanology and Geothermal Research, 53(1-4), 47-66.

472 Reid, M. E., Sisson, T. W., & Brien, D. L. (2001). Volcano collapse promoted by hydrothermal alteration
473 and edifice shape, Mount Rainier, Washington. Geology, 29(9), 779-782.
474 Reid, M. E. (2004). Massive collapse of volcano edifices triggered by hydrothermal
475 pressurization. Geology, 32(5), 373-376.

476

477 Rincón, M., Márquez González, Á., Van Wyk de Vries, B., Herrera, R., Granja Bruña, J. L., & Llanes

478 Estrada, P. (2015). Aplicación del sensor Kinect en modelos análogos para la identificación morfo-

479 estructural de procesos de deformación en volcanes.

480

481 Rincón, M., Márquez, A., Herrera, R., Alonso-Torres, A., Granja-Bruña, J. L., & van Wyk de Vries, B.

482 (2018). Contrasting catastrophic eruptions predicted by different intrusion and collapse scenarios. Scientific

483 reports, 8(1), 1-11.

484

485 Rincón, M., Márquez, A., Herrera, R., Galland, O., Sánchez- Oro, J., Concha, D., & Montemayor, A. S.

486 (2022). Monitoring Volcanic and Tectonic Sandbox Analogue Models using the Kinect v2 Sensor. Earth

487 and Space Science, e2020EA001368.

488

489 Rivera, M., Thouret, J. C., Mariño, J., Berolatti, R., & Fuentes, J. (2010). Characteristics and management

490 of the 2006–2008 volcanic crisis at the Ubinas volcano (Peru). Journal of Volcanology and Geothermal

491 Research, 198(1-2), 19-34.

492

493 Rosas-Carbajal, M., Komorowski, J. C., Nicollin, F., & Gibert, D. (2016). Volcano electrical tomography

494 unveils edifice collapse hazard linked to hydrothermal system structure and dynamics. Scientific

495 reports, 6(1), 1-11.

496

497 Salaün, A., Villemant, B., Gérard, M., Komorowski, J. C., & Michel, A. (2011). Hydrothermal alteration

498 in andesitic volcanoes: trace element redistribution in active and ancient hydrothermal systems of

499 Guadeloupe (Lesser Antilles). Journal of Geochemical Exploration, 111(3), 59-83.

500

501 Samaniego, P., Valderrama, P., Mariño, J., van Wyk de Vries, B., Roche, O., Manrique, N., ... & Malnati,

502 J. (2015). The historical (218±14 aBP) explosive eruption of Tutupaca volcano (Southern Peru). Bulletin

503 of Volcanology, 77(6), 1-18.

504

505 Seisdedos, J., Ferrer, M., & de Vallejo, L. G. (2012). Geological and geomechanical models of the pre-

506 landslide volcanic edifice of Güímar and La Orotava mega-landslides (Tenerife). Journal of volcanology

507 and geothermal research, 239, 92-110.

508

509 Sekiya, S. and Y. Kikuchi (1890) : The eruption of Bandai-san Journal of the College of Science, Imperial

510 University, Japan, 3 91-172

511

512 Siebert, L., Glicken, H., & Ui, T. (1987). Volcanic hazards from Bezymianny-and Bandai-type

513 eruptions. Bulletin of Volcanology, 49(1), 435-459.

514

515    Siebert, L. (1992). Threats from debris avalanches. Nature, 356, 658-659

516

517    Shirzaei, M., Walter, T. R., Nankali, H. R., & Holohan, E. P. (2011). Gravity-driven deformation of
518    Damavand volcano, Iran, detected through InSAR time series. Geology, 39(3), 251-254.

519

520    Solikhin, A., Thouret, J. C., Gupta, A., Harris, A. J., & Liew, S. C. (2012). Geology, tectonics, and the
521    2002–2003 eruption of the Semeru volcano, Indonesia: Interpreted from high-spatial resolution satellite
522    imagery. Geomorphology, 138(1), 364-379.

523

524    Thouret, J. C., Rivera, M., Wörner, G., Gerbe, M. C., Finizola, A., Fornari, M., & Gonzales, K. (2005).
525    Ubinas: the evolution of the historically most active volcano in southern Peru. Bulletin of
526    Volcanology, 67(6), 557-589.

527

528    van Wyk de Vries, B., & Francis, P. W. (1997). Catastrophic collapse at stratovolcanoes induced by gradual
529    volcano spreading. Nature, 387(6631), 387-390.

530

531    van Wyk de Vries, B., & Matela, R. (1998). Styles of volcano-induced deformation: numerical models of
532    substratum flexure, spreading and extrusion. Journal of Volcanology and Geothermal Research, 81(1-2), 1-
533    18.

534

535    van Wyk de Vries, B., Kerle, N., & Petley, D. (2000). Sector collapse forming at Casita volcano,
536    Nicaragua. Geology, 28(2), 167-170.

537

538    Van Wyk de Vries, B., Márquez, A., Herrera, R., Bruña, J. L., Llanes, P., & Delcamp, A. (2014). Craters
539    of elevation revisited: forced-folds, bulging and uplift of volcanoes. Bulletin of Volcanology, 76(11), 1-20.

540

541    Van Wyk de Vries, B., & de Vries, M. V. W. (2018). Tectonics and volcanic and igneous plumbing systems.
542    In Volcanic and igneous plumbing systems (pp. 167-189). Elsevier.

543

544    Voight, B., Janda, R. J., Glicken, H., & Douglass, P. M. (1983). Nature and mechanics of the Mount St
545    Helens rockslide-avalanche of 18 May 1980. Geotechnique, 33(3), 243-273.

546

547    Voight, B., Komorowski, J. C., Norton, G. E., Belousov, A. B., Belousova, M., Boudon, G., ... & Young,
548    S. R. (2002). The 26 December (Boxing Day) 1997 sector collapse and debris avalanche at Soufriere Hills
549    volcano, Montserrat. Geological Society, London, Memoirs, 21(1), 363-407.

550

551    Zimbelman, D., Watters, R. J., Bowman, S., & Firth, I. (2003). Quantifying hazard and risk assessments at
552    active volcanoes. Eos, Transactions American Geophysical Union, 84(23), 213-217.

**FIGURES**

**Fig 1** Experimental setup. (A) type S volcano spreading by hydrothermal core and (B) Type I cryptodome intrusion. A tripod with the Kinect sensor attached is located at a height of 0.75 meters above the table with the experiment. The data obtained by the Kinect sensor is sent in real time to a data computing system

**Fig 2** Sketches of the different experiments produced by the combination of simulated hydrothermal system parameters (shape, size, and location). The combination resulting for a hypothetical experiment S8 (in red) is logistic impossible

**Fig 3** Results from spreading by hydrothermal core experiments (type S). Variation of the distance images at time t3 (3 minutes in the experiment ~ 30,000 years in nature), with the deformation structures overlaid. Lines a-b show the location of the profiles of figure 4

**Fig 4** Red line: topographic profiles of the S-type experiments at time t3 (3 minutes in the experiment ~ 30,000 years in nature), compared with initial experiment profiles (black line). Grey figures: weak-core geometry at the starting of the experiment

**Fig 5** Results from cryptodome intrusion experiments (type I). Variation of the distance image from time t20 (20 minutes in the experiment ~ 25 days in nature), with the deformation structures overlaid. Lines a-b show the location of the profiles of figure 6

**Fig 6** Two representative examples of type I experiments. Red line: topographic profiles at time t20 profile (20 minutes in the experiment ~ 25 days in nature) compared with initial experiment profiles (black line)

**Fig 7** Sketches of the characteristics fault patterns and topographic changes (subsidence in blue, uplift in red) detected at (A) Spreading experiment when the hydrothermal core is centred (B) Cryptodome intrusion when the tube intrusion is centred (deformation pattern 1 of Rincón et al. 2018) (C) Spreading experiment when the hydrothermal core is off – centred and (D) Cryptodome intrusion when the tube intrusion is off-centred (deformation pattern 3 of Rincón et al. 2018)

578    **Fig 8** Topographic profiles (from SRTM and Aster-DEM data) of studied natural cases of stratovolcanoes

579    showing potential flank deformation due to edifice asymmetric spreading over a weak hydrothermally-

580    altered core. Red line marks the location of the proposed flank bulge analysed at each case

581

582    **TABLES**

583    **Table 1** Scaling: Geometrical and mechanical parameters of scaling and their values in nature and model
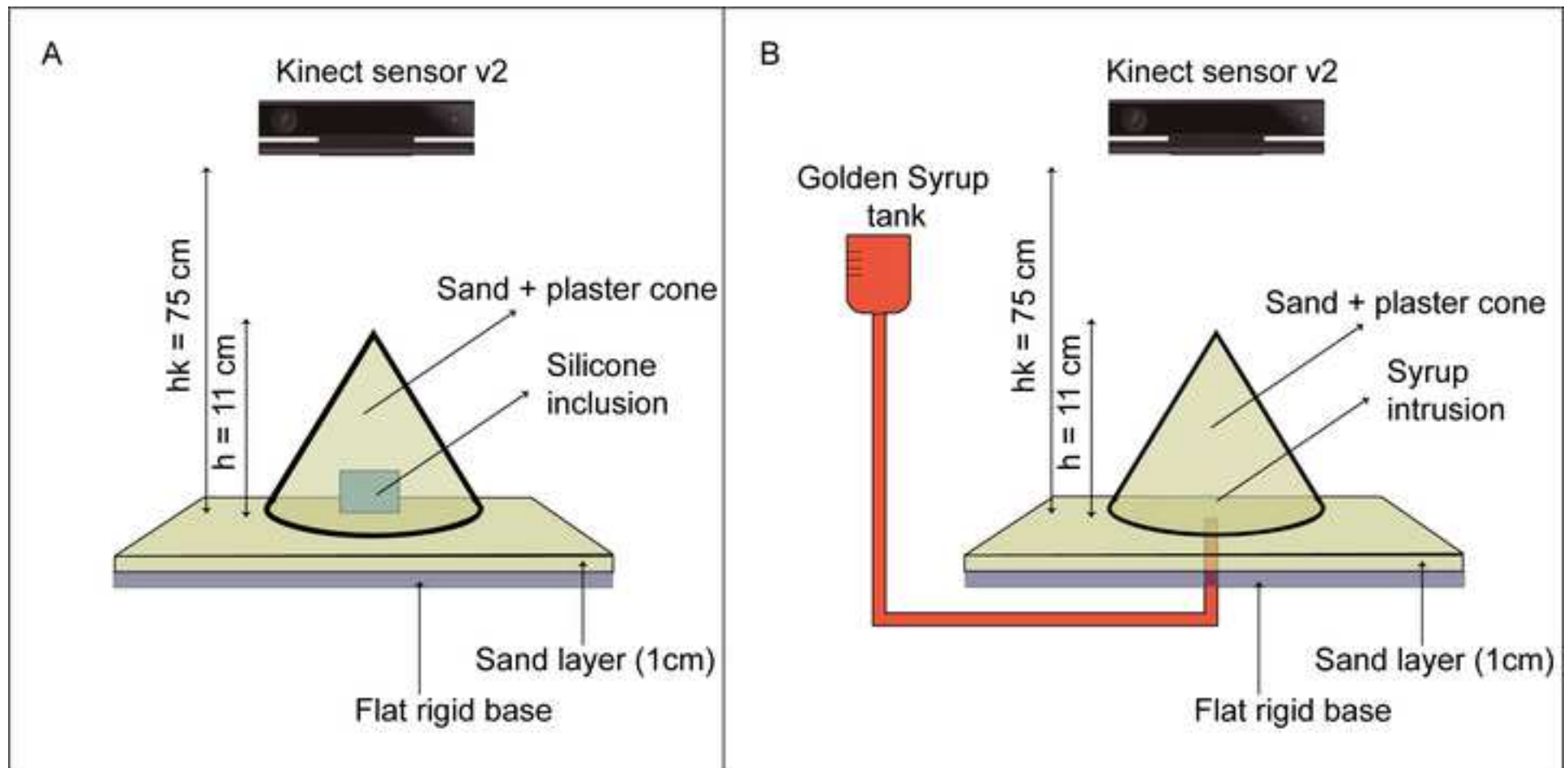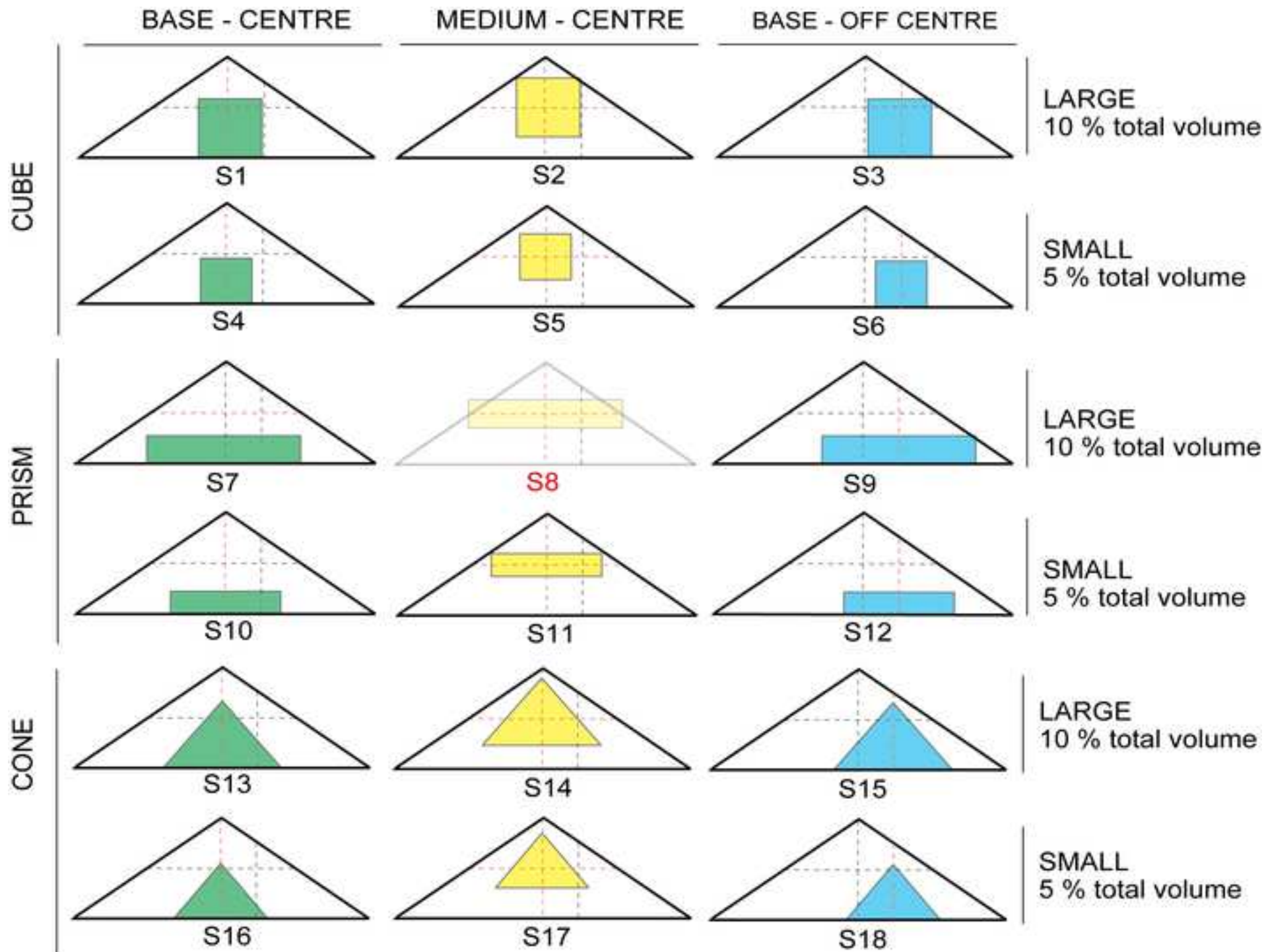
584

585
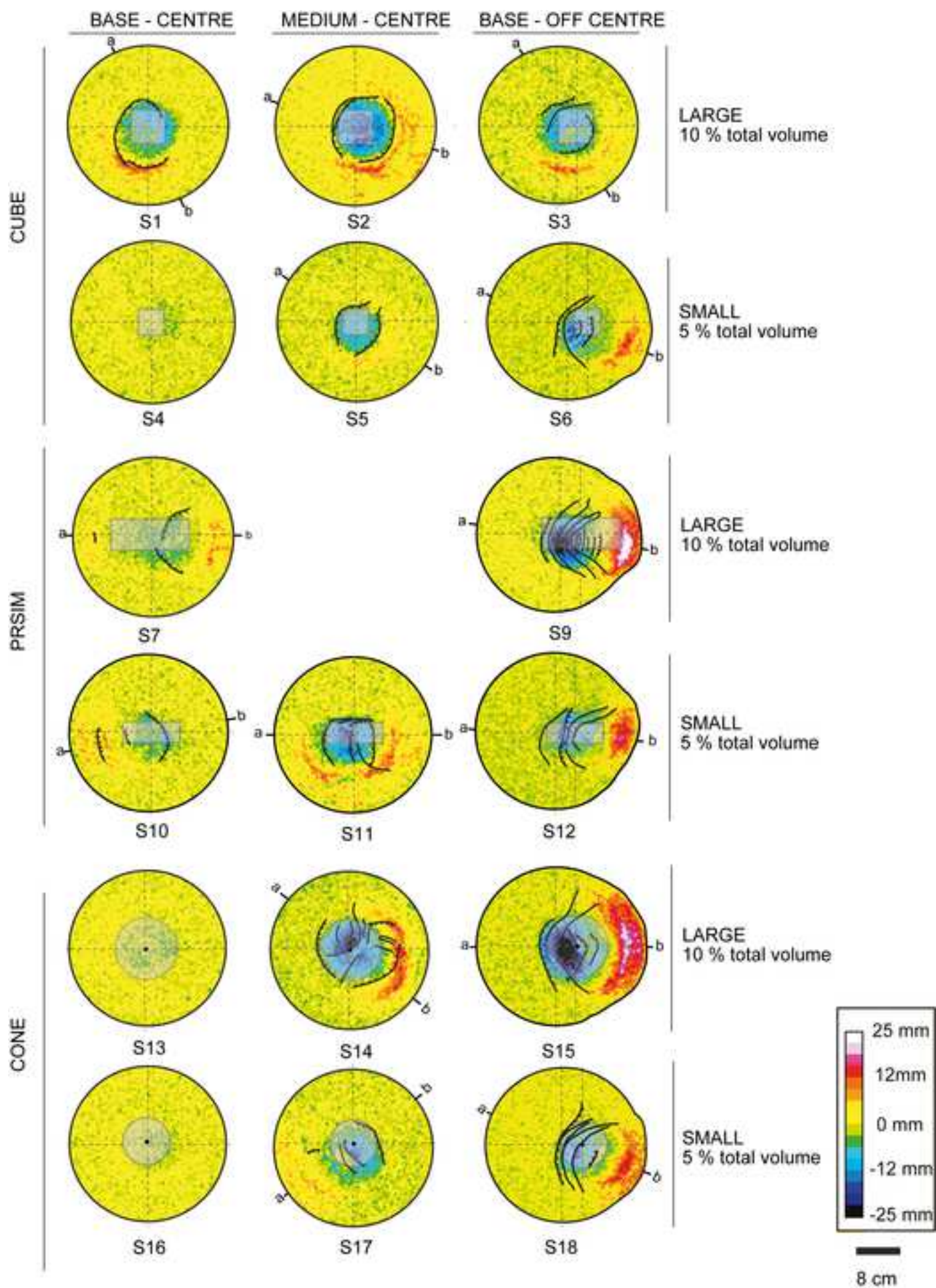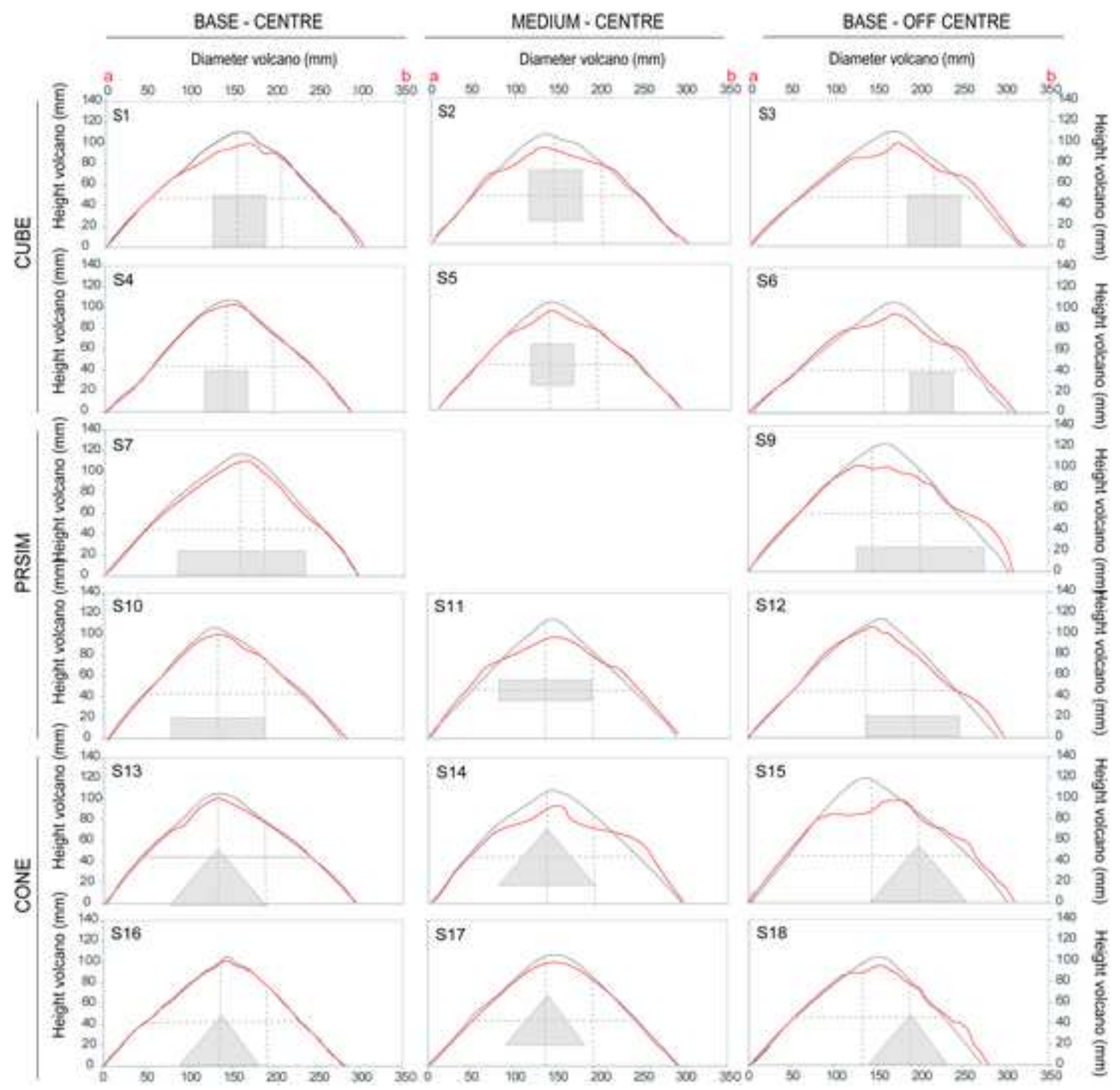
Figure 1

Figure 1

Figure 2

Click here to access/download;Figure;Fig2.tif

Figure 3

Click here to access/download;Figure;Fig3.tif



BASE - CENTRE | MEDIUM - CENTRE | BASE - OFF CENTRE

CUBE

S1  S2  S3  LARGE 10 % total volume

S4  S5  S6  SMALL 5 % total volume

PRSIM

S7  S9  LARGE 10 % total volume

S10  S11  S12  SMALL 5 % total volume

CONE

S13  S14  S15  LARGE 10 % total volume

S16  S17  S18  SMALL 5 % total volume

25 mm
12mm
0 mm
-12 mm
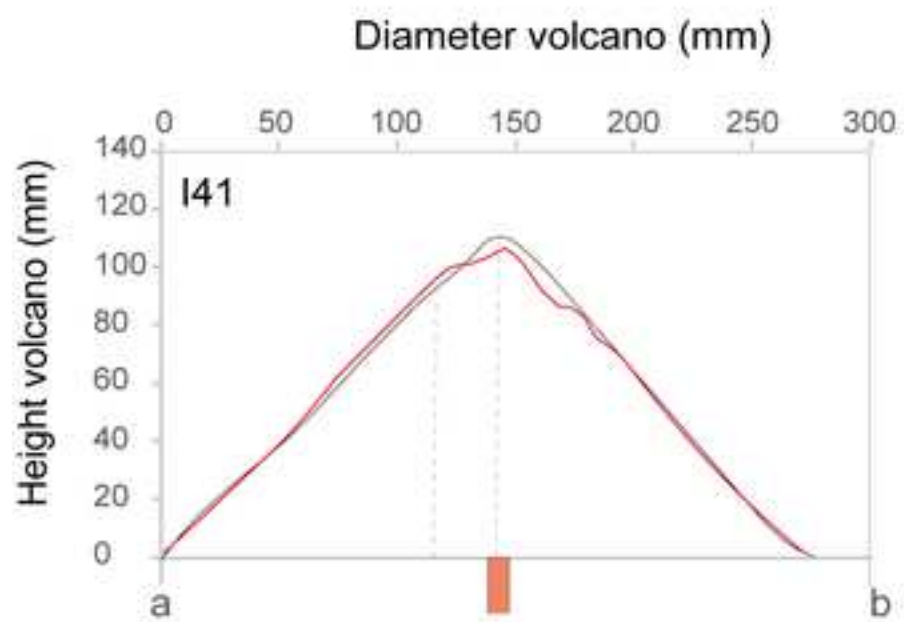-25 mm

8 cm

Figure 4

Figure 5

```
Your image file "Fig 5.tif" cannot be opened and processed.  Please see
the common list of problems, and suggested resolutions below.

Reason:  The image file is corrupt or invalid.  Please check and
resubmit.

Other Common Problems When Creating a PDF from an image file
----------------------------------------------------------------

You will need to convert your image file to another format or fix the
current image, then re-submit it.
```
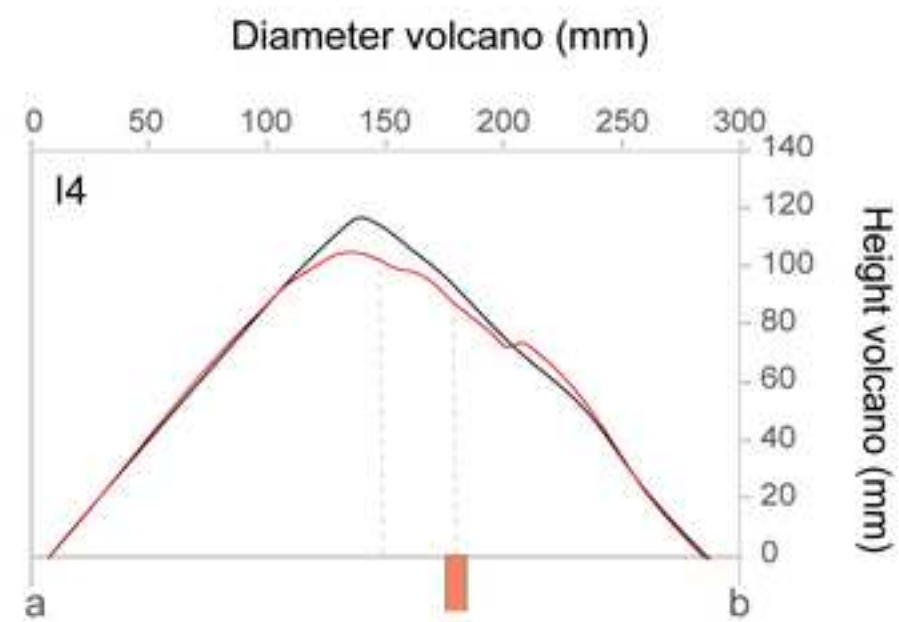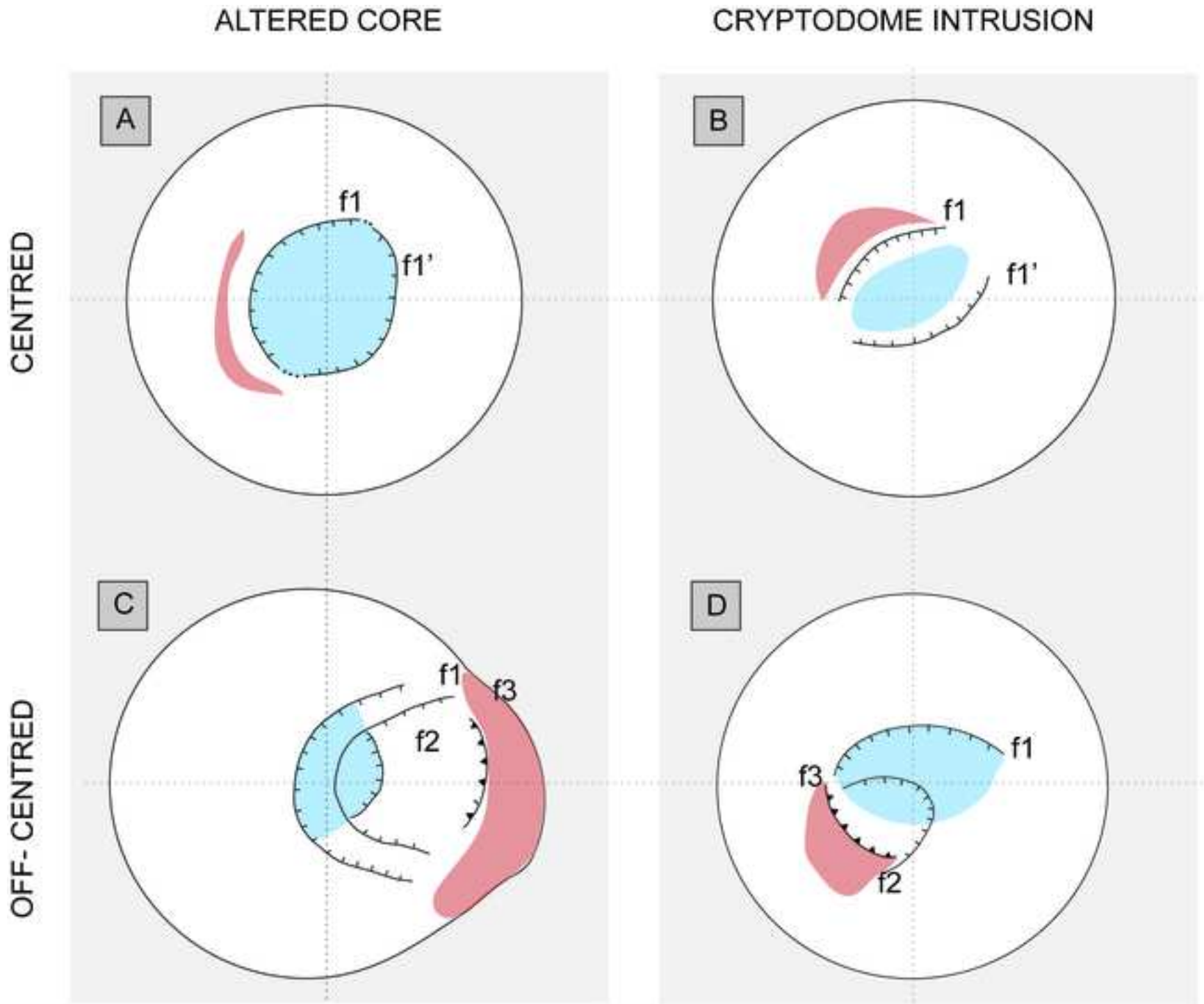
Figure 6

Click here to access/download;Figure;Fig6.tif ⬇



CENTRE INTUSION

Diameter volcano (mm)

OFF CENTRE INTRUSION

Diameter volcano (mm)

Figure 7

Click here to access/download;Figure;Fig7.tif ⬇



ALTERED CORE

CRYPTODOME INTRUSION

CENTRED

OFF- CENTRED

A

f1
f1'

B

f1
f1'

C

f1
f3
f2

D

f1
f3
f2

Figure 8

Figure 8
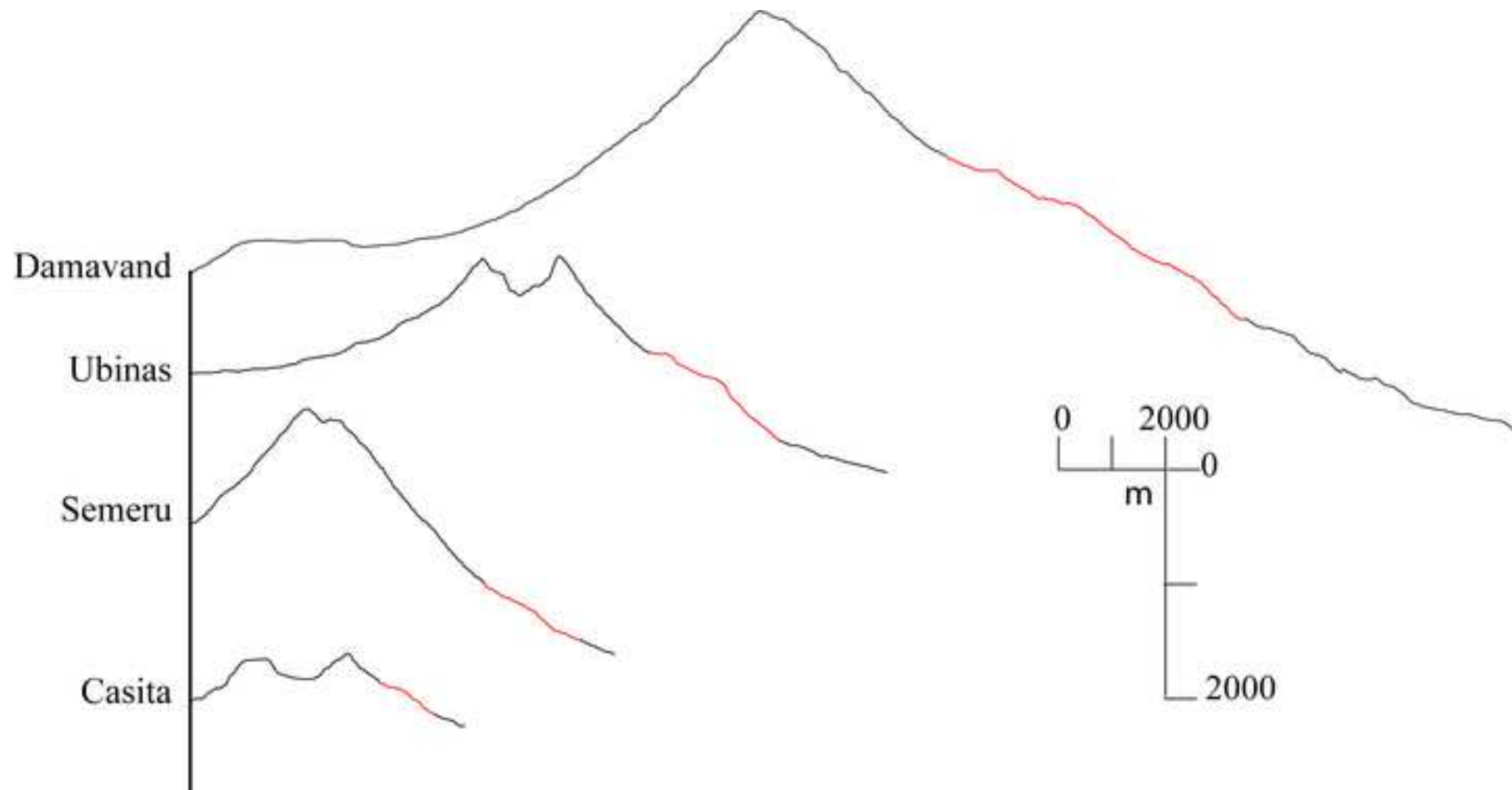
Table 1

| Parameters | Definition | Model (M) | Nature (N) | Ratio (M/N) | Units (IS) | Dimensions |
|---|---|---|---|---|---|---|
| h | Stratovolcano Height | 0.11 | 1100 | $1\times10^{-4}$ | M | [L] |
| R | Stratovolcano radius | 0.15 | 15000 | $1\times10^{-5}$ | M | [L] |
| g | Gravity | 1 | 1 | 1 | $m\times s^{-2}$ | $[LT^{-2}]$ |
| $\rho_v$ | Stratovolcano density | 1320 | 2500 | $5.5\times10^{-1}$ | $kg\ m^{-3}$ | $[M\times L^{-3}]$ |
| $\sigma_v$ | Stratovolcano cohesion | 50 - 100 | $9\times10^5$ | $2.5\times10^{-6}$ | $kg\times m^{-1}$ | $[M\times L^{-1}]$ |
| $\Phi$ | Friction angle | 36-37 | 36-37 | 1 | ° | - |
| ts | Deformation time spreading | 0-600 | $0 - 3.2\times10^{12}$ | $0 - 1.9\times10^{-10}$ | S | [T] |
| ti | Deformation time intrusion | 0-1.200 | $0 - 2.2\times10^6$ | $0 - 5.5\times10^{-4}$ | S | [T] |
| $\mu_{sh}$ | Hydrothermal core viscosity | $1\times10^4$ | $1\times10^{18}$ | $1\times10^{-15}$ | $kg\times m^{-1}\times s^{-2}$ | $[M\times L^{-1}\times T^{-2}]$ |
| $\mu m$ | Magma viscosity | 30 | $1.5\times10^9$ | $3.3\times10^{-9}$ | $kg\times m^{-1}\times s^{-2}$ | $[M\times L^{-1}\times T^{-2}]$ |
| Qm | Magma flow | $1.7\times10^9$ | 1-100 | $1.5\times10^9$ | $m^{-3}\times s$ | $[L^{-3}\times T^{-1}]$ |

Click here to access/download
**Supplementary Material**
ESM1.pdf